On temperature inversions and the mesospheric surf zone

F. Sassi, R. R. Garcia, B. A. Boville, and H. Liu
National Center for Atmospheric Research, Boulder, Colorado, USA

Received 19 November 2001; revised 28 February 2002; accepted 28 February 2002; published 5 October 2002.

[1] Mesospheric thermal inversions are investigated in a numerical simulation with the Whole Atmosphere Community Climate Model, an upward extension of the National Center for Atmospheric Research's Community Climate Model. The seasonal character, spatial extent, and magnitude of the inversion layers are realistic during winter. In the model, the occurrence of wintertime inversions is a direct consequence of the rapid decay with height of vertically propagating planetary waves, which induces large temperature perturbations in the upper mesosphere to maintain hydrostatic equilibrium. The magnitude of the inversions is highly correlated with planetary wave amplitude, so that large inversions develop during episodes of planetary wave amplification. Gravity waves do not play a major direct role in the formation of the inversions because the largest thermal tendencies associated with gravity wave breaking occur well above the range of altitudes where inversions are found. However, gravity waves play an essential indirect role because they set up a critical line in the upper mesosphere where Rossby waves break in the mesospheric surf zone. *INDEX TERMS:* 3332 Meteorology and Atmospheric Dynamics: Mesospheric dynamics; 3334 Meteorology and Atmospheric Dynamics: Middle atmosphere dynamics (0341, 0342); 3319 Meteorology and Atmospheric Dynamics: General circulation; 3384 Meteorology and Atmospheric Dynamics: Waves and tides; *KEYWORDS:* temperature inversions, planetary waves

Citation: Sassi, F., R. R. Garcia, B. A. Boville, and H. Liu, On temperature inversions and the mesospheric surf zone, *J. Geophys. Res.*, *107*(D19), 4380, doi:10.1029/2001JD001525, 2002.

1. Introduction

[2] In midlatitudes during winter, planetary-scale Rossby waves transfer momentum from the lower atmosphere, where they are excited, to higher levels, where they dissipate. Wave breaking [*McIntyre and Palmer*, 1984] is one of the principal mechanisms of planetary wave dissipation, and it leads to the formation of distinct surf zones in the subtropical stratosphere and mesosphere [*Gille and Lyjak*, 1984; *Dunkerton and Delisi*, 1985; *Garcia*, 1991]. *Dunkerton and Delisi* [1985] noted that the sequence of events leading to sudden warmings and momentum deposition in the stratosphere is not always accompanied by similar events in the mesosphere. In fact, the stratospheric and mesospheric surf zones behave somewhat independently.

[3] The stratospheric surf zone is formed when planetary waves are refracted equatorward by the polar night jet and eventually encounter a critical line near low latitudes where they are absorbed. (For quasistationary waves, the critical line is defined by the locus of points in the latitude-height plane where $\bar{u} = 0$.) Planetary waves that propagate into the upper mesosphere encounter a critical line near 75 km at middle and high latitudes, resulting in the formation of a mesospheric surf zone between about 70 and 80 km. The existence of a critical line in the upper mesosphere is due to deposition of easterly momentum by small-scale gravity waves [*Matsuno*, 1982; *Holton*, 1983; *Garcia and Solomon*, 1985]. Gravity waves of zonal phase velocity $\lesssim 10\ \mathrm{ms}^{-1}$ can propagate through the polar night jet in the stratosphere, and break at altitudes above 60 km, decelerating the jet and actually reversing the zonal circulation above 75 km. Without gravity waves, this upper mesospheric critical line would not exist, and planetary waves would be dissipated through a deep layer in the mesosphere and lower thermosphere, producing a surf zone extending well above 100 km [*Garcia*, 1991; *Garcia et al.*, 1992]. Thus, the compact character of the mesospheric surf zone is ultimately dictated by interactions between gravity waves and planetary waves.

[4] The mesospheric surf zone appears to be associated with wintertime "inversions" of the mesospheric temperature profile. Lidar observations [*Schmidlin*, 1976; *Hauchecorne et al.*, 1987; *Meriwether et al.*, 1994] have shown that the thermal structure of the mesosphere can occasionally show warm layers, which interrupt the otherwise uniform decrease of temperature with height, and have come to be known as "mesospheric inversion layers." A complete explanation of the processes that lead to mesospheric inversions does not exist at present; however, observations have shown that mesospheric inversions are ubiquitous, both in time and space, so it is unlikely that a single explanation exists for all the manifestations of the phenomenon. Lidar observations indicate that, although inversions are stronger in winter, they can also occur during summer [*Hauchecorne et al.*, 1987], and in the tropics as well as at higher latitudes [*Leblanc et al.*, 1995]. Similarly, satellite

0148-0227/02/2001JD001525$09.00

observations [*Leblanc et al.*, 1995; *Leblanc and Hauchecorne*, 1997] show that thermal inversion layers are found at many locations, but preferentially near midlatitudes in winter. Several mechanisms have been proposed to explain the inversion layers: Gravity wave heating [*Hauchecorne et al.*, 1987], diabatic heating by the downwelling branch of the mean meridional circulation [*Hauchecorne and Maillard*, 1990], tidal and gravity wave temperature perturbations [*Bills and Gardner*, 1993; *Meriwether et al.*, 1998], and the interaction between vertically propagating gravity waves and tidal winds [*Liu and Hagan*, 1998] have all received considerable attention.

[5] More recently, satellite observations have shown that planetary wave dissipation in the upper winter mesosphere is accompanied by thermal inversion layers immediately below the dissipation region [*Wu*, 2000; *Salby et al.*, 2001]. These studies suggest that the formation of mesospheric inversions in winter and planetary wave dissipation in the upper mesosphere are closely related. In order to study the relationship among planetary waves, wave dissipation, and mesospheric thermal inversions, we have used a new model developed at the National Center for Atmospheric Research (NCAR). The Whole Atmosphere Community Climate Model (WACCM) extends the NCAR Community Climate Model (CCM3) upward to the lower thermosphere using physical parameterizations appropriate for this region obtained from the Thermosphere-Ionosphere-Mesosphere Electrodynamics GCM (TIME/GCM) [*Roble and Ridley*, 1994]. A description of WACCM is presented in section 2. Mesospheric thermal inversions resembling closely those observed at midlatitudes during winter are found in a numerical simulation. The seasonal cycle and general character of the modeled inversions is discussed in section 3, and their relationship to the mesospheric surf zone is elucidated in section 4. To highlight the role of gravity waves, we contrast in section 5 the base simulation to a simulation wherein the gravity wave parameterization used in WACCM is replaced by a Rayleigh friction layer. Conclusions are presented in section 6.

2. Model Description

[6] WACCM is based on the NCAR Community Climate Model, version 3 (CCM3), which has been described in detail by *Kiehl et al.* [1998a]. WACCM is run with 66 vertical levels from the surface to about 140 km. Vertical resolution is $\leq$1.5 km between the tropopause and about 25 km. Above that altitude, vertical resolution increases slowly to 2 km at the stratopause and 3.5 km in mesosphere; beyond the mesopause, the vertical resolution is one half the local scale height. The horizontal resolution is T63, with 128 $\times$ 64 points in a quasilinear grid [*Williamson*, 1997]. The dynamical equations are solved using a semi-Lagrangian technique [*Williamson and Olson*, 1994] with a time step of 1800 s.

[7] The climate produced by the standard 18-level of CCM3 version is discussed by *Hack et al.* [1998], *Hurrell et al.* [1998], and *Kiehl et al.* [1998b]. Although CCM3 produces a fairly realistic climate in the lower atmosphere, for simulations extending above the stratosphere the model needs to be complemented by additional physical processes appropriate to the upper atmosphere:

- In addition to the parameterization of orographic (stationary) gravity waves, a parameterization of a spectrum of traveling gravity waves is implemented. Both parameterizations are based on *Lindzen*'s [1981] formulation. A spectrum of gravity waves is launched at 100 hPa, including phase velocities in the range [−40, +40] m s^{-1}, at intervals of 10 m s^{-1}. The phase velocities are oriented in the direction of the wind at the source level. The stress at the source level has a Gaussian dependence on the phase speed,

$$\tau(c) = \tau_0 \exp\left[\left(-\frac{c}{30}\right)^2\right], \quad (1)$$

where c is the phase speed, and τ_0 is the stress at the source corresponding to a stationary gravity wave ($c = 0$).

- The CCM3 longwave radiation code does not include non-LTE effects, which become important in the mesosphere. These are taken into account by adopting the parameterization of *Fomichev et al.* [1998], which calculates non-LTE longwave heating in the 15-μm band of CO_2 and the 9.6-μm band of O_3. Following *Fomichev and Blanchet* [1995], in WACCM the CCM3 longwave radiation code is used exclusively below 60 km, and the Fomichev scheme above 70 km. The two longwave parameterizations are merged between 60 and 70 km, where the heating rates calculated by each match closely. The resulting vertical structure of longwave heating (not shown) is smooth and continuous throughout the transition region.
- In the upper mesosphere and lower thermosphere, absorption of solar radiation at wavelengths <200 nm by the Schumann-Runge bands and continuum of O_2 is the primary shortwave heating mechanism. Since CCM3 was not designed to study the upper atmosphere, it calculates solar heating longward of 200 nm only. Therefore, in WACCM the CCM3 shortwave heating rates are merged with those calculated using the shortwave parameterization from the NCAR TIME-GCM [*Roble and Ridley*, 1994]. The procedure is similar to that used for longwave heating: The CCM3 and TIME-GCM parameterizations are used exclusively below 60 km and above 70 km, respectively. In the range of altitudes 60–70 km, the two calculations are merged, producing a smooth shortwave heating profile throughout the entire 0–140 km domain of WACCM.
- Molecular viscosity is an important process that determines the dynamical and thermal structure of the atmosphere above about 100 km. In WACCM, a parameterization based on the treatment of *Banks and Kockarts* [1973] is used. Momentum and temperature are diffused assuming a mean atmosphere where nitrogen and oxygen remain the major constituents with constant mixing ratio throughout the model's range of altitudes. This assumption is not completely justified near the top boundary of the model, but results in the upper 15–20 km are not expected to be realistic, since this range of altitudes is designed to control upward wave propagation.
- In the thermosphere, ionized species become abundant and interact with the geomagnetic field resulting in a force acting on the neutral wind that becomes significant above ~120 km. A parameterization of this so-called ion drag, based on the work of *Dickinson et al.* [1975], is employed in WACCM.

[8] For this study, we utilize results from the second year of a 20-year simulation, although the behavior discussed

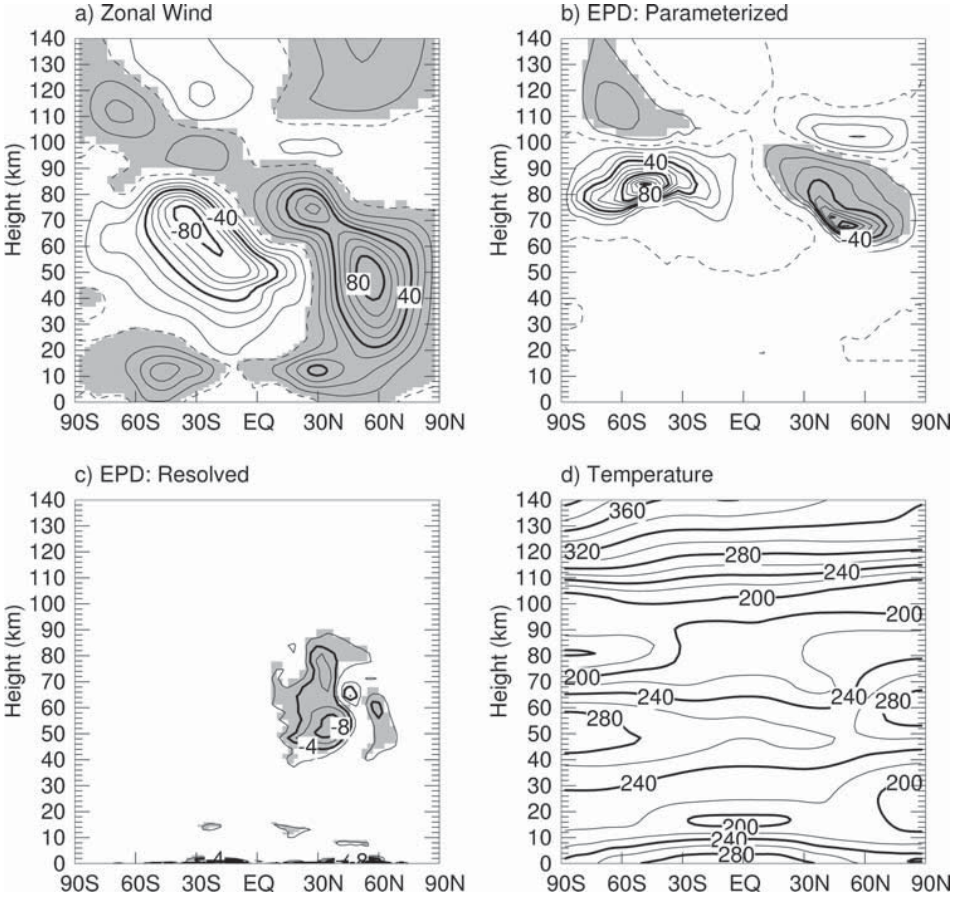

Figure 1. January averages for the base simulation. (a) Zonal-mean zonal wind (m s^{-1}); the contour interval is 10 m s^{-1}, the zero-wind line is dashed, and shading denotes positive values. (b) Zonal-mean zonal momentum tendency due to nonstationary gravity waves (m s^{-1} day^{-1}); the contour interval is 5 m s^{-1} day^{-1}, the zero contour is dashed, and shading denotes negative values. (c) Zonal-mean zonal momentum tendency due to resolved waves (m s^{-1} day^{-1}); the contour interval is 2 m s^{-1} day^{-1}, and shading denotes negative values. (d) Zonal mean temperature (K); the contour interval is 10 K.

below is not specific to that particular year. Figure 1 shows the zonal mean state averaged for January. The westerly jet in the winter hemisphere (Figure 1a) tilts equatorward as a result of deposition of easterly gravity wave momentum in the upper mesosphere (Figure 1b). From the upper mesosphere to the lower thermosphere, the gravity wave parameterization produces alternating regions of easterly and westerly zonal mean acceleration. A similar pattern, but of opposite sign, is found in the summer hemisphere. The alternating layers of zonal mean acceleration give rise to corresponding layers of alternating zonal winds, with reversals (i.e., zero-wind lines) occurring at about 70–80 km and 110 km at winter midlatitudes. The zonal structure of Figure 1a reproduces observations [e.g., *McLandress et al.*, 1996] reasonably well.

[9] The Eliassen-Palm flux divergence due to explicitly resolved waves (mainly planetary-scale Rossby waves) shows regions of enhanced wave dissipation in the subtropical stratosphere, and in the subtropical and midlatitude mesosphere of the winter hemisphere (Figure 1c). The resulting zonal mean acceleration is largely easterly, as expected of Rossby waves, and is due in large part to wave breaking. (An exception is the small region between 35 and 65 km, poleward of 50°N, where the waves undergo thermal dissipation.) The largest sources of easterly accelerations are found near 30°N in both the stratosphere and mesosphere. In the mesosphere, significant accelerations are also present in midlatitudes, extending to about 60°N. The regions of enhanced dissipation in the stratosphere and mesosphere are "surf zones," as described by *McIntyre and Palmer* [1984]. Note that the mesospheric surf zone is compact: It is confined to altitudes below 90 km, maximizing near 80 km, and extending between about 30°N and 60°N in this particular model month.

[10] The temperature field (Figure 1d) shows a slight thermal inversion, even in the zonal mean, at northern midlatitudes near 70 km. The inversion occurs near the location of the peak planetary wave amplitude in the mesosphere (not shown). However, the two-dimensional model study of *Hauchecorne and Maillard* [1990] suggests that planetary waves are not essential for producing these small inversions in the zonal mean temperature profile; the behavior can be due solely to adiabatic warming by the mean meridional circulation driven by gravity wave breaking. Nonetheless, it must be emphasized that the amplitude of the zonal mean inversion displayed in Figure 1d is only a

few K, whereas the inversions observed locally by lidar on any given night of observation are typically much larger (20–40 K).

3. Temporal and Latitudinal Distribution of Mesospheric Inversions

[11] Thermal inversions in the mesosphere have been detected throughout the year in data from the Rayleigh lidar of the Observatoire de Haute Provence (OHP) [*Hauchecorne et al.*, 1987]. The magnitude of the inversions (measured as the temperature difference between the top and the bottom of the inversion layer) is largest during local winter, when thermal inversions often exceed 20 K and the bottom of the inversion layer is located most frequently between 60 and 70 km. Inversion amplitudes of up to 40 K are observed occasionally. The annually varying magnitude of inversion layers is smallest around May. In summertime, mesospheric inversion layers are found about 5–10 km higher than during winter, their magnitude being considerably smaller as well.

[12] Lidar data have good vertical resolution (~1 km) but, as with any single-profile measurement, they lack information on global behavior. On the other hand, satellite data from the Upper Atmosphere Research Satellite (UARS) [*Leblanc et al.*, 1995; *Leblanc and Hauchecorne*, 1997; *Wu*, 2000; *Salby et al.*, 2001] and from the Solar Mesosphere Explorer (SME) [*Clancy et al.*, 1994] have been used to document the global structure of the mesospheric inversion layers. It should be noted that the nature of satellite sampling can impact the quality of those observations. In particular, the limited vertical resolution of the satellite measurements reduces the apparent amplitude of the inversion layers, whose depth in the lidar data is typically 10–15 km. Nevertheless, the overall structure of the annual cycle emerging from satellite observations is in agreement with the OHP data. In addition, satellite observations show clearly that the mesospheric inversions have large spatial scale, often extending over several thousand kilometers in longitude and latitude. The inversions seen in the satellite data tend to persist for several days, a behavior that is also seen in the OHP lidar observations [cf., e.g., *Wu*, 2000, Figure 6; *Hauchecorne et al.*, 1987, Figure 1].

[13] Satellite observations detect inversions of largest amplitude during solstice at middle and high latitudes [*Leblanc et al.*, 1995; *Wu*, 2000]. The midlatitude mesospheric inversions show a pronounced annual variation, which has been ascribed by Leblanc et al. to filtering of gravity waves by the polar night jet in the stratosphere. At low latitudes, thermal inversions show a strong semiannual cycle [*Leblanc and Hauchecorne*, 1997], which *Clancy et al.* [1994] have attributed to the mesospheric semiannual oscillation (SAO). The mean amplitude of the equinoctial inversions in the tropics appears to be much larger in Clancy et al.'s SME data (30–40 K) than in Leblanc and Hauchecorne's UARS data (8–10 K). A possible explanation for this difference is that SME made observations at a fixed local time, which would have resulted in aliasing of the diurnal tide onto the SME zonal mean temperature estimates. Since the amplitude of the diurnal tide is known to have a strong semiannual variation [e.g., *Sassi and Salby*, 1999], it is possible that the equinoctial inversions observed by SME are due in part to the temperature signal associated with the tide.

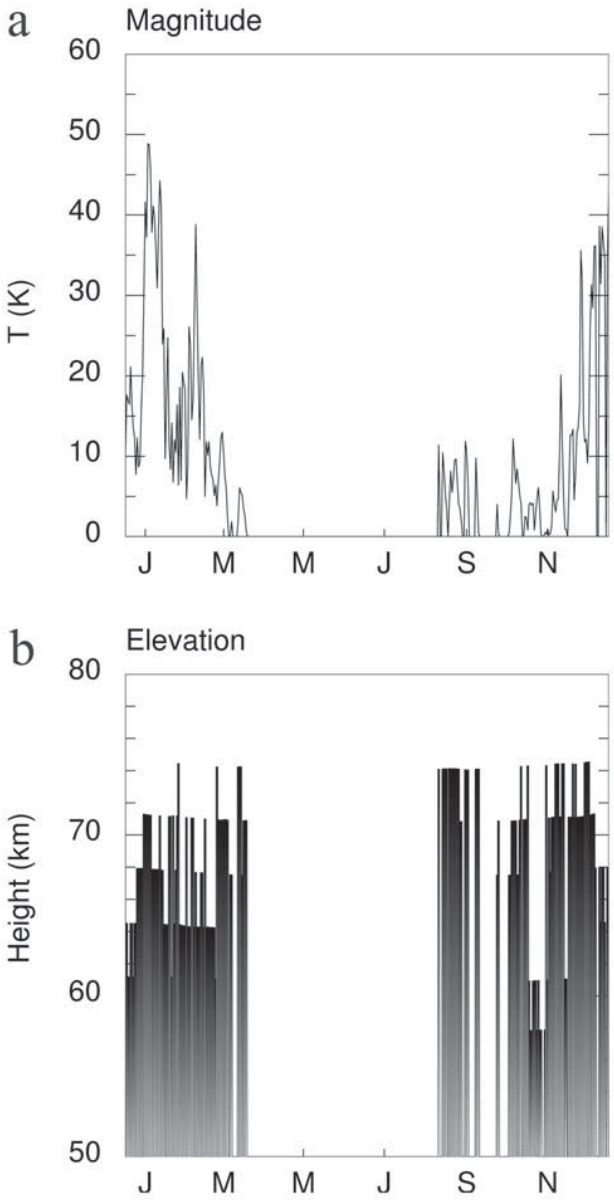

Figure 2. Annual variation of (a) daily amplitude (K) of mesospheric thermal inversions near 0°E and 43°N and (b) the altitude (km) of the base of the inversions. The amplitude is defined as the temperature difference between the top and the bottom of the inversion layer; the altitude is defined as the height of the base of the inversion.

[14] In summary, satellite and ground-based data together yield a consistent picture of the spatial and temporal distribution of mesospheric inversions. Inversion layers are detected during all seasons and at all latitudes; however, they are larger and more frequent during winter in midlatitudes, where they occur at altitudes between 60 and 75 km.

[15] Thermal inversions are also found in the annual simulation using WACCM. They are most clearly defined around the winter solstice, and they exhibit an annual cycle similar to that observed. This is illustrated by Figure 2,

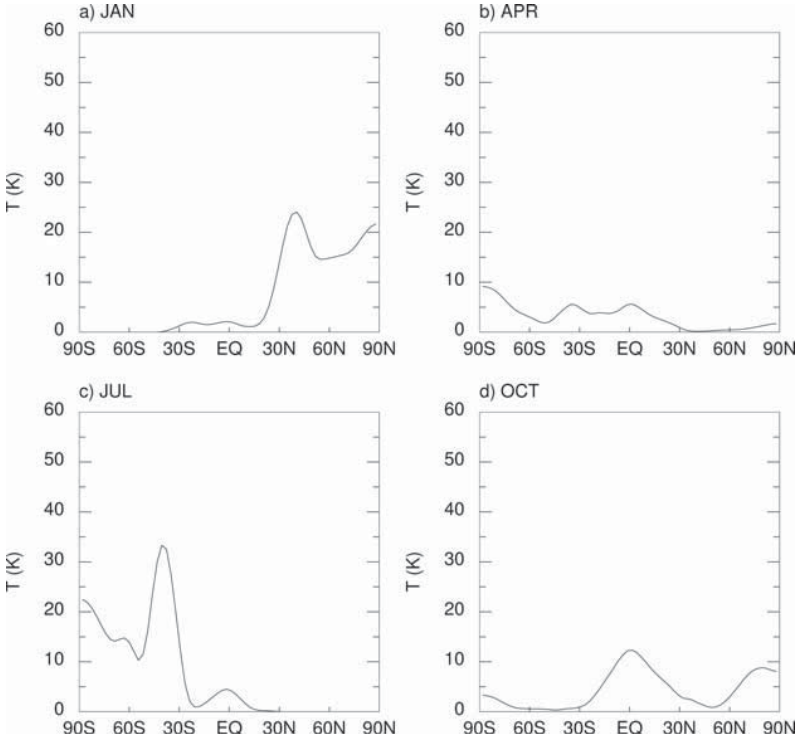

Figure 3. Global distribution of mesospheric inversion amplitude (K) in (a) January, (b) April, (c) July, and (d) October. The value plotted is akin to a zonal average except that those longitudes where inversion layers are absent (i.e., where the temperature actually decreases with height) are assigned zero amplitude.

which shows the amplitude of thermal inversions and altitude of the inversion base on a daily basis for an atmospheric column near 43°N and 6°E (near the location of OHP). The base of the thermal inversion is identified with the level of minimum temperature in mesosphere, when that location is clearly distinct from the altitude of the mesopause. The magnitude of thermal inversions is obtained as the temperature difference between the top of the inversion layer and its base. The amplitude of the inversions (Figure 2a) increases during winter, with the largest event found near the middle of January ($\Delta T \simeq 45$ K). Most of the inversions in Figure 2a have an amplitude of 20–30 K during winter. The magnitude of thermal inversions decreases as the year advances to around 10 K during spring. Thermal inversions disappear altogether at this location near the end of May. Inversion layers of about 10 K reappear intermittently in early fall, and more frequently (and with larger amplitude) as winter approaches once more.

[16] With few exceptions, the base of the mesospheric inversions (Figure 2b) produced by the model lies between 65 and 75 km. Thermal inversions in early fall (September) are of small amplitude and appear to be associated with the transition between the summertime and wintertime temperature profiles at this altitude. That is, as summer ends, the altitude of the midlatitude mesopause rises from near 80 km to about 100 km (compare the temperature distribution in the summer and winter hemispheres shown in Figure 1). During this transition, the model temperature profile often exhibits double mesopauses, near 80 and 100 km. This behavior is discussed in more detail in the next section, where it is contrasted to that of temperature inversions produced by the model in midwinter.

[17] The monthly-averaged latitudinal distribution of mesospheric inversions in WACCM is shown in Figure 3. During January (Figure 3a) and July (Figure 3c), inversion layers are found throughout the winter hemisphere extratropics, with distinct peaks at middle and high latitudes. The amplitude of tropical mesospheric inversions in the model is generally small, but approaches 10 K during the equinoxes. In fact, during October (Figure 3d) the amplitude of the inversions is largest at the equator. At midlatitudes, the character of the annual cycle shown in Figure 3 is consistent with the lidar and satellite observations mentioned above, except for the complete disappearance of inversions in the model during summer. The winter inversions observed from satellites are about 2–4 times smaller than what is calculated with WACCM. As noted previously, this is to be expected given the limited vertical resolution of satellite observations. On the other hand, the large amplitude of thermal inversions in the simulation is quite consistent with lidar data, whose finer vertical resolution captures the thermal inversion layers more clearly.

4. Morphology of Midlatitude Winter Inversions

[18] The features shown in Figures 2 and 3 indicate that the temporal and geographical distribution and the amplitude of midlatitude mesospheric inversions in winter are well represented in WACCM. The spatial structure of the inversions is best described by a combination of ground-based and satellite data. The lidar data of Hauchecorne and

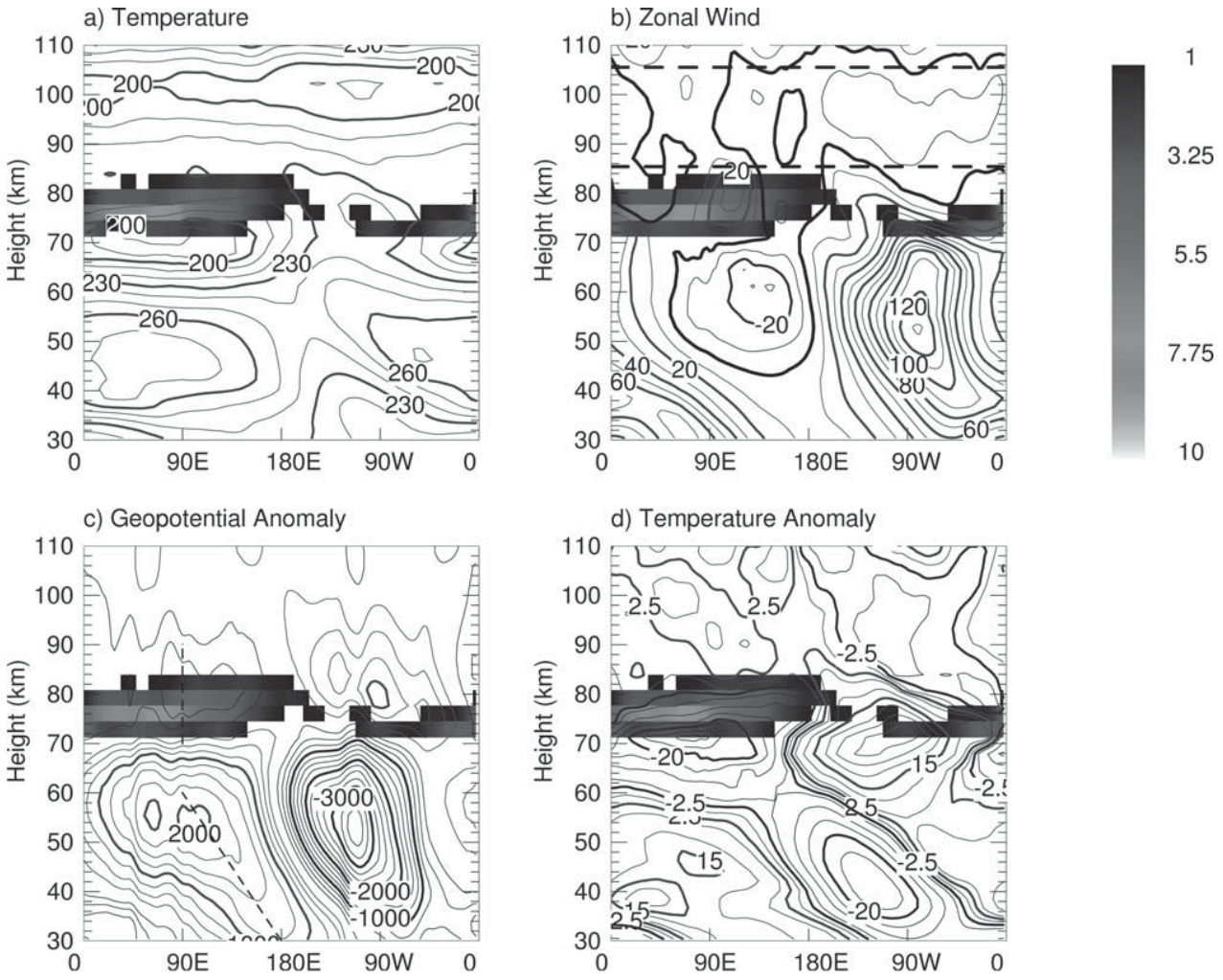

Figure 4. Model fields (height-longitude sections) for 21 January at 43°N. (a) Temperature (K); contour interval is 10 K. (b) Zonal wind (m s^{-1}); contour interval is 10 m s^{-1}, and the thick black dashed line denotes the location of the zonal-mean zero-wind line; the thick black solid line denotes the local zero-wind line. (c) Geopotential anomaly (m); contour interval is 250 m, and the black dashed lines highlight the phase tilt with height. (d) Temperature anomaly (K); contour interval is 2.5 K. In all plots, the vertical gradient of total temperature T_z is indicated by color shading; the color scale is shown on the right.

colleagues, discussed in the previous section, at OHP are representative of high vertical resolution lidar observations and document clearly the vertical structure of the inversion layers. As regards the horizontal extent of the inversions, the coordinated lidar measurements at OHP (44°N, 5°E) and Centre d'Essais des Landes (44°N, 1°W) described by *Leblanc and Hauchecorne* [1997] show that they can extend over at least several hundred kilometers in longitude.

[19] In fact, the synoptic view offered by satellite observations shows clearly that the inversions extend over very large areas. *Wu* [2000] has investigated the midlatitude winter events using data from the Microwave Limb Sounder (MLS) onboard the Upper Atmosphere Research Satellite and found that mesospheric inversions often occur simultaneously over a broad belt of middle and high latitudes, and at each latitude they extend over many degrees of longitude. The inversions are also found to correlate well with episodes of planetary wave amplification, and occur at altitudes in the upper mesosphere where the vertical structure of planetary waves changes from propagating to evanescent. As noted by Wu and discussed in detail by *Salby et al.* [2001], this abrupt shift in geopotential amplitude gives raise to strong temperature perturbations, T', which are related to the geopotential, Φ', by the hydrostatic equation,

$$T' = (H/R)\Phi'_z, \tag{2}$$

where R is the gas constant of dry air, H is the atmospheric scale height, and subscript z indicates vertical derivative.

[20] Using daily averaged output (thus filtering the diurnal tide), Figure 4 illustrates the relationship between planetary waves and mesospheric inversions in WACCM, showing that the inversions produced by the model during winter resemble closely the observations. In all panels of Figure 4 the locations where the vertical gradient of temperature is positive ($T_z > 0$) in the mesosphere are indicated by color shading. Figure 4a shows contours of temperature as a function of longitude and height at 43°N on 21 January.

(This is the closest latitude in the model to the location of OHP, where many observations of mesospheric inversions have been recorded.) Temperature increases throughout the stratosphere with the warmest temperature (270 K) found at about 50 km. Temperature begins to decrease above the stratopause at all longitudes, but the vertical gradient is then reversed near 70 km; this reversal is strongest in the zonal sector west of 90°E and rather weak between 180°E and 90°W. The vertical temperature gradient, T_z, is about 7.5 K km^{-1} near 75 km at about 60°E, where temperatures continue to increase up to 85 km. Above this altitude the temperature field recovers the zonally uniform decrease typical of the mesosphere, with the mesopause found around 100 km.

[21] Figure 4b shows latitude-height contours of zonal wind. The strong zonal westerlies of the stratosphere weaken in the upper mesosphere, reversing at most longitudes above 80–85 km. Another wind reversal, this time from easterly to westerly, is found near 105 km. (The thick dashed lines denote the locations where the zonal-mean zonal wind, $\bar{u}$, is zero.) The strongest thermal inversion layer (centered at about 60°E) occurs over a range of longitudes where stratospheric winds are relatively weak and are overlain by weak easterly winds in the lower mesosphere. Such a vertical wind profile would be expected to filter out much of the spectrum of vertically propagating gravity waves. Thus, the suggestion of *Leblanc et al.* [1995] that gravity waves play a direct role in the development of mesospheric inversions is not borne out in the WACCM simulation.

[22] In fact, the zonal wind in midlatitudes is approximately in geostrophic equilibrium,

$$u = -\frac{1}{af}\frac{\partial \Phi}{\partial \theta}, \tag{3}$$

where f is the Coriolis parameter, a is the radius of the Earth, and θ is latitude. Because the peak amplitude of the geopotential anomaly in the model is located near 50°N, the longitudinal structure of the zonal wind at the latitude of OHP (43°N) is approximately out of phase with the structure poleward of 50°N, by equation (3). Nevertheless, the model produces strong mesospheric inversions at both 43°N (Figure 4) and poleward of 50°N (not shown). This is further evidence that filtering of gravity waves is not the mechanism responsible for producing mesospheric inversions in the model.

[23] Figure 4c shows the geopotential anomaly (i.e., the deviation from zonal average) in the model. The anomaly is dominated by zonal wavenumber 1, and exhibits the westward tilt characteristic of vertically propagating Rossby waves throughout the stratosphere and lower mesosphere. Above about 65 km the phase of the geopotential anomaly ceases to change with height, indicating that the wave field is no longer vertically propagating. The change occurs a couple of scale heights below the altitude of the critical line for quasistationary waves in the zonal mean wind ($\bar{u} = 0$, compare Figure 4a). The presence of the critical line results in both wave absorption and reflection, so that a standing wave pattern of sharply reduced amplitude is set up everywhere above 65 km.

[24] Figure 4d shows the zonal anomaly in temperature. Temperature is approximately in quadrature with geopotential (Figure 4c) throughout the stratosphere and lower mesosphere, where the wave pattern is vertically propagating. Above 65–70 km, temperature and geopotential are out of phase, consistent with the evanescent nature of the waves in the upper mesosphere. The very fast decay of the geopotential field between 65 and 75 km produces large temperature anomalies in the same range of altitude, consistent with hydrostatic equilibrium, equation (2). In particular, the large negative anomaly centered near 60°E and 70 km gives rise to the inversion seen in the total temperature field of Figure 4a.

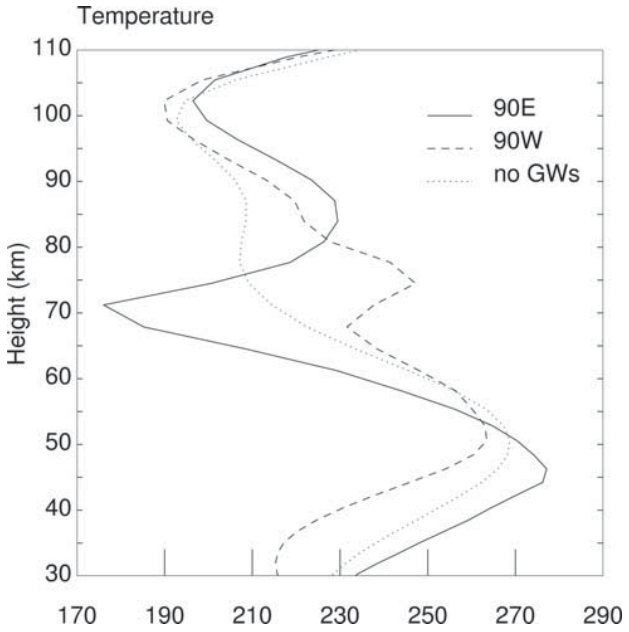

Figure 5. Vertical profiles of temperature (K) calculated with the model at 43°N on 21 January at 90°E (solid line) and 90°W (dashed line). Also shown is the January average profile at 43°N and 90°W for a model run without parameterized gravity waves (dotted line). See text for details.

[25] Figure 5 displays vertical profiles of temperature at 90°E and 90°W for the same inversion event as shown in Figure 4 (the profile labeled "no GWs" is actually a profile from a run without the spectrum of parameterized gravity waves; it is discussed separately in section 5). At 90°E, temperature decreases steeply in the mesosphere up to 70 km, that level coinciding with the coldest temperature anomaly seen in Figure 4d. This temperature minimum represents the bottom of the inversion layer, which extends upward to about 85 km; the temperature difference between the bottom and top of the inversion is about 45 K. Note that this strong mesospheric thermal inversion occurs atop the cold temperature anomaly (compare Figure 4b). In the opposite phase of the wave (centered near 90°W), the thermal inversion is weak. At this longitude, the main effect of the wave is to raise the temperature throughout much of the mesosphere. Clearly, the variation of inversion amplitude with longitude is a direct consequence of the phase of the upward propagating wave field on the particular day illustrated in Figures 4 and 5. However, insofar as the planetary wave field of the Northern Hemisphere has a

strong stationary component, one would expect to find the strongest temperature inversions most frequently in the eastern hemisphere. In fact, we have examined numerous other cases of wintertime inversions produced by the model and found behavior similar to that shown in Figure 4.

[26] It is worth noting that the structure of the quasistationary planetary wave field produced in the model is in agreement with observations. The temporal average of geopotential calculated from MLS temperature measurements (not shown) has a pattern similar to that of Figure 4c. However, closer inspection of the MLS observations reveals the presence of a significant traveling wave component. Mesospheric inversions thus appear intermittently at different location in these observations [*Salby et al.*, 2001]. In WACCM, the traveling wave component is considerably weaker than in observations, and mesospheric inversions occur predominantly in the longitude sector west of 90°E.

[27] As suggested by Figure 4, wintertime inversions obtained with WACCM are very strongly related to the structure of the quasistationary planetary wave field. Indeed, we find that the combined amplitude of waves 1 and 2 in the mesosphere is an excellent predictor of the magnitude of mesospheric thermal inversions in the model. This is illustrated in Figure 6, which shows the behavior of mesospheric inversions on a daily basis at 43°N and 90°E (the location of the strongest inversion layer in Figure 4) during the first 60 days of the model year, together with the largest combined amplitude attained by planetary waves 1 plus 2 between 60 and 80 km. The amplification of the waves during the second half of January (days 15 through 30) is mirrored by an increase in the amplitude of thermal inversions, which become largest around 20 January. During the remainder of the period shown, both the amplitude of wave temperature and thermal inversions decrease in concert.

[28] It was noted in section 3 that the inversions produced by WACCM in early fall appear to be related to the transition between summer and winter temperature regimes. Examination of the calculated temperature structure at 43°N for September does not reveal the presence of strong wave perturbations such as shown in Figure 4. Instead, a vertical profile with minima near 75–80 km and 95–100 km is obtained at most longitudes (Figure 7). These altitudes are typical of the summertime and wintertime mesopause, respectively, at this latitude. Figure 7 thus suggests that the weak midlatitude inversions produced by WACCM in September are not wave phenomena, but a reflection of the remnants of the summer temperature profile together with the incipient development of the winter profile.

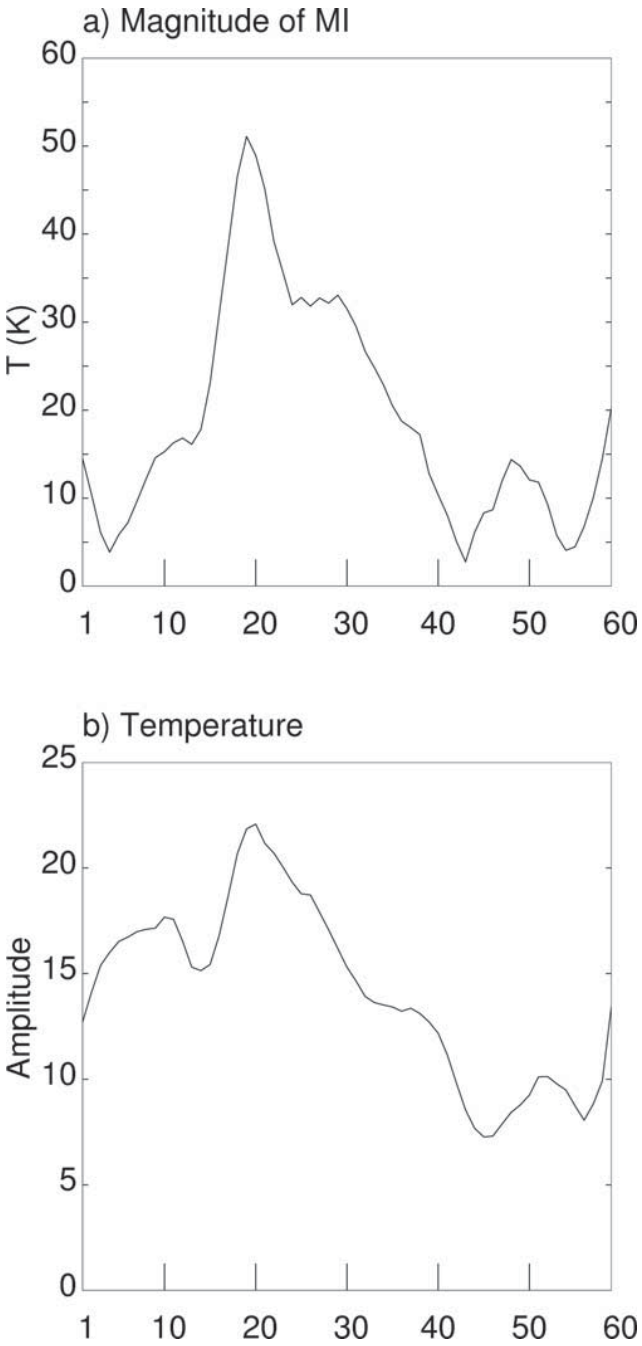

Figure 6. (a) Daily amplitude (K) of mesospheric thermal inversions at 43°N and 90°E during the first 60 days of the model year (day 0 is 1 January). (b) Largest amplitude of the combined wavenumber 1 plus wavenumber 2 thermal anomaly (K) between 60 and 80 km.

5. Role of Gravity Waves

[29] We have shown that the occurrence of mesospheric thermal inversions in WACCM is closely associated with amplification and breaking of planetary-scale Rossby waves. Such wave breaking occurs in the mesospheric surf zone, whose location and extent are determined by the position of the critical line ($\bar{u} = 0$), which in the model is ultimately maintained by the dissipation of parameterized gravity waves.

[30] Planetary wave breaking results in a down-gradient flux of potential vorticity, or any other tracer having a meridional gradient. The spatial distribution of this down-gradient flux is illustrated in Figure 8, which shows the horizontal diffusion coefficient (K_{yy}) calculated using the orthogonal-tracers method of *Plumb and Mahlman* [1987]. In this method, two tracers are initialized as sine of latitude and vertical level index, respectively, and are advected for 1 month by the model winds, with a small relaxation toward their initial values to keep their distributions from becoming colinear. Diffusion coefficients are then obtained by relating

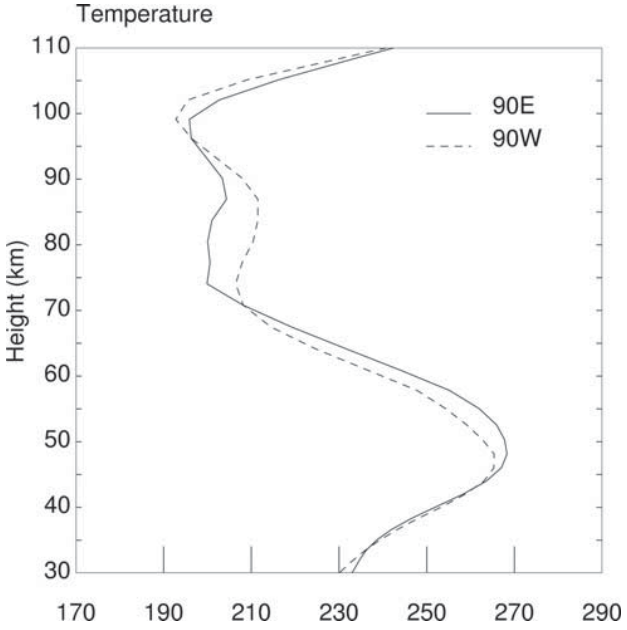

Figure 7. Vertical profiles of temperature (K) calculated with the model at 90°E, 43°N (solid line) and 90°W, 43°N (dashed line) on 17 September.

eddy fluxes computed from the resolved fields to the zonal mean gradients of the tracers, as discussed by Plumb and Mahlman. The diffusion coefficients shown in Figure 8 are calculated from monthly averaged fields during January. Large values of K_{yy} are calculated near locations of large EP flux divergence in the subtropical stratosphere and midlatitude upper mesosphere (compare Figure 1c). These two regions constitute the stratospheric and mesospheric surf zones, respectively.

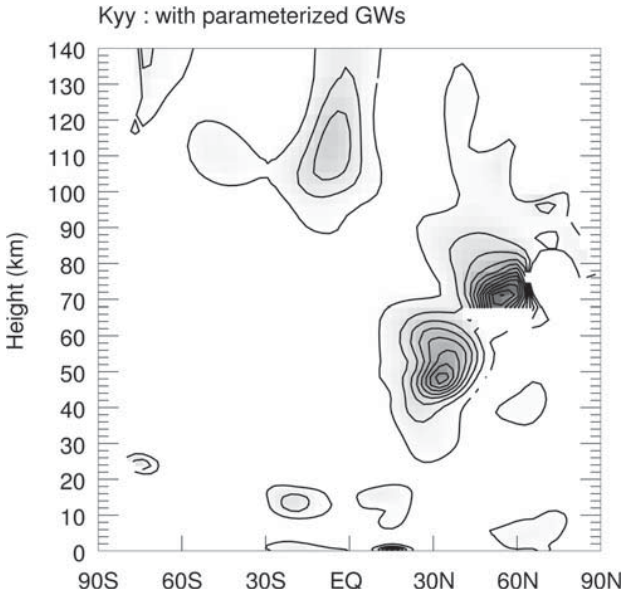

Figure 8. Horizontal diffusion coefficient (m^2 s^{-1}) calculated from the orthogonal tracer method of *Plumb and Mahlman* [1987]. The contour interval is 2×10^6; the first contour is 1×10^6. See text for details.

[31] To elucidate the influence of the parameterized gravity wave spectrum on the pattern of planetary wave breaking in WACCM, we carried out a simulation wherein that parameterization was removed. In order to keep the stratospheric jets from growing continuously with altitude, a Rayleigh friction layer was introduced above 80 km, with friction coefficient approaching a maximum of 1 day^{-1} above about 100 km. Figure 9 shows the zonal mean zonal wind for this simulation. Note, in particular, that there is no zero-wind line anywhere in the upper mesosphere; in the winter hemisphere, the polar night jet extends to the upper boundary of the model, although its magnitude decreases above about 60 km. A direct consequence of this wind distribution is that planetary waves break throughout the mesosphere and lower thermosphere, rather than in a narrow range of altitude in the mesosphere, as was the case in the standard run. This is illustrated in Figure 10, which shows K_{yy} for the model simulation without parameterized gravity waves. In contrast to the standard results shown in Figure 8, there is now a broad region of large K_{yy} extending from the stratosphere through the lower thermosphere. From the point of view of the waves, the entire atmosphere equatorward and above the polar night jet behaves as one continuous surf zone.

[32] The gradual decrease of wave amplitude with height in the run without parameterized gravity waves does not produce strong thermal anomalies like that shown in Figure 4 for the standard case. Figure 11 illustrates this by showing the anomalies of geopotential and temperature during 20 January of the simulation without gravity waves. Both fields show a uniform decrease of amplitude with height. There is little indication of the wave becoming evanescent below 100 km. As a consequence, the temperature field does not develop thermal inversions at any longitude even though large amplitude planetary waves are present in this case also. The dotted curve in Figure 5 shows a typical vertical temperature profile for the run without gravity waves. The contrast with the

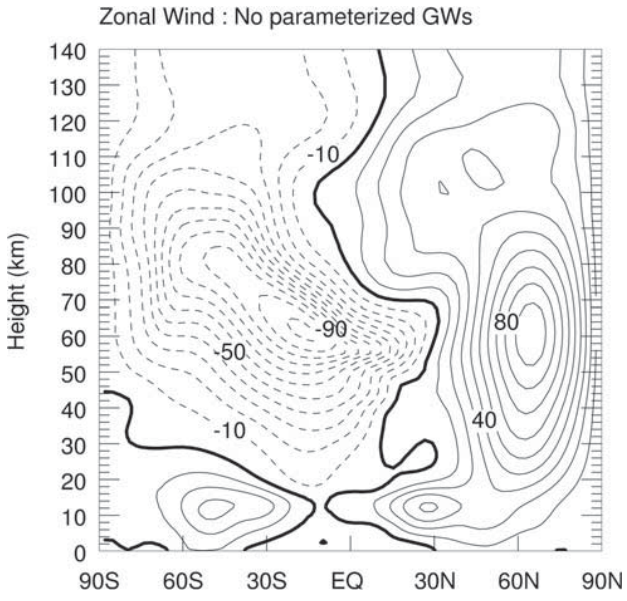

Figure 9. As in Figure 1a, but for the simulation without parameterized gravity waves.

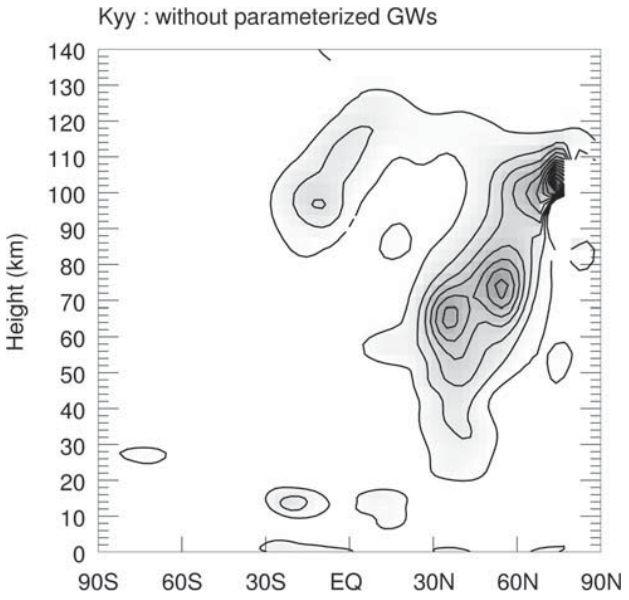

Figure 10. As in Figure 8, but for the simulation without parameterized gravity waves.

profiles obtained in the standard simulation, also shown in Figure 5, is striking.

6. Conclusions

[33] We have used the Whole Atmosphere Community Climate Model (WACCM) to show that episodes of wintertime planetary wave amplification and breaking in the midlatitude upper mesosphere can produce thermal inversions, where temperature increases by about 20–25 K on average in a 10 km layer. In the model simulations discussed in this paper, the inversions are a direct consequence of the rapid dissipation of planetary waves in the mesospheric surf zone. This surf zone is found in midlatitudes and is rather compact, extending over the altitude range 70–80 km. The amplitude of vertically propagating planetary waves diminishes rapidly as the waves approach the surf zone, and this gives rise, through hydrostatic equilibrium, to very large temperature anomalies in the upper mesosphere. Mesospheric temperature inversions are then found to occur in phase with the negative wave temperature anomaly in the upper mesosphere, which constitutes the base of the inversion layer (Figure 4).

[34] The mesospheric inversions modeled in this study are long-lived, corresponding to observed inversions that persist over several days. Thus, neither tides nor high-frequency gravity waves play a role in producing these phenomena. Because mesospheric inversions in WACCM are instead closely related to the dissipation of planetary waves, the strongest inversions are found in association with episodes of planetary wave amplification (Figure 6). Although we have discussed in detail only the boreal winter season, the model produces similar results during austral winter. Thermal inversions in boreal winter occur preferentially in the zonal sector centered near 90°E. This is a result of the large amplitude of the quasistationary wave field in the model. The phase structure of these waves is such that they give rise to a deep temperature minimum (the base of the mesospheric inversions) in a sector of longitude centered near 60°E.

[35] Gravity waves do not play a significant direct role in the thermal inversions produced by the model. In fact, the heating due to kinetic energy dissipated by the spectrum of parameterized gravity waves is small compared to the temperature anomalies associated with mesospheric thermal inversions. However, parameterized gravity waves are the dominant forcing in the mesospheric momentum budget and play an essential indirect role in setting up a critical line for quasistationary Rossby waves in the upper mesosphere. The presence of this critical line leads to the formation of a compact mesospheric surf zone, and hence to the rapid dissipation of vertically propagating planetary waves that is essential for producing thermal inversions in the model. This conclusion is confirmed by a simulation that omits parameterized gravity waves. In this case, the winter polar night jet extends without reversals to the top boundary of the model, a compact mesospheric surf zone does not

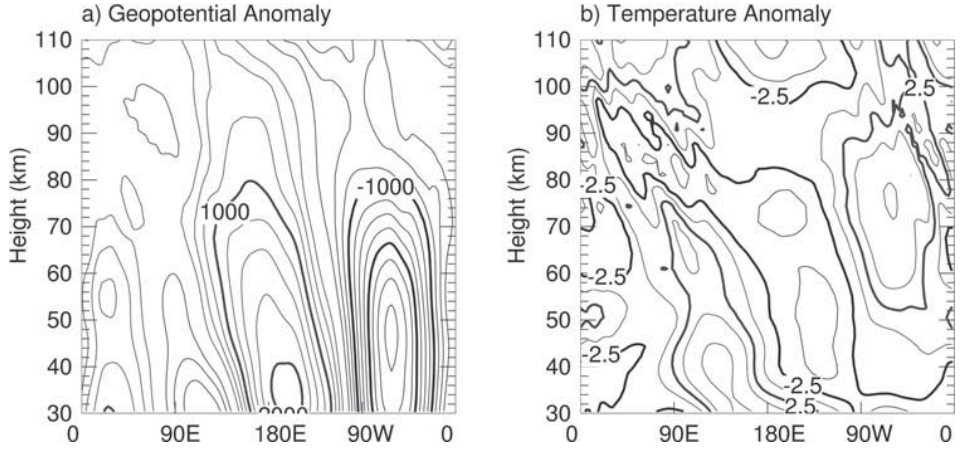

Figure 11. Model fields (height-longitude sections) at 59°N for 20 January, from the run without parameterized gravity waves. (a) Geopotential anomaly (m); contour interval is 250 m. (b) Temperature anomaly (K); the contour interval is 2.5 K.

develop, and planetary waves are dissipated throughout a deep layer in the upper mesosphere and lower thermosphere. Such gradual dissipation is unable to produce large temperature anomalies so that the wintertime mesospheric inversions largely disappear.

[36] In agreement with observations, midlatitude thermal inversions in WACCM are most frequent during winter solstice but, contrary to observations, they vanish completely during the summer months. WACCM also produces small mesospheric inversions in the tropics (Figure 3), most frequently at the equinoxes and, especially, around the fall equinox. These occur near 80 km, in association with a (warm) westerly shear layer that overlies the mesospheric SAO easterlies (not shown). However, this wind structure is not very realistic; in particular, the model produces westerlies above the mesospheric easterlies at equinox, something that is not observed [*Garcia et al.*, 1997]. Thus, the calculations presented here provide a robust, physically plausible mechanism for the formation of mesospheric inversions at midlatitudes during winter. However, the source of summertime inversions, and of inversions occurring in the tropics, requires further study.

[37] **Acknowledgments.** The National Center for Atmospheric Research is sponsored by the National Science Foundation. The development of WACCM has been supported in part by the NCAR Director's Opportunity Fund. The authors thank M. Hagan and A.K. Smith for their comments.

References

Banks, P. M., and G. Kockarts, *Aeronomy*, part B, 355 pp., Academic, San Diego, Calif., 1973.

Bills, R. E., and C. S. Gardner, Lidar observations of the mesosphere region temperature structure at Urbana, *J. Geophys. Res.*, *98*, 1011–1021, 1993.

Clancy, R. T., D. W. Rusch, and M. T. Callan, Temperature minima in average thermal structure of the middle atmosphere (70–80 km) from analysis of 40- to 92-km SME global temperature profiles, *J. Geophys. Res.*, *99*, 19,001–19,020, 1994.

Dickinson, R. E., E. C. Ridley, and R. G. Roble, Meridional circulation in the thermosphere, I, Equinox conditions, *J. Atmos. Sci.*, *32*, 1737–1754, 1975.

Dunkerton, T. J., and D. P. Delisi, The subtropical mesospheric jet observed by the Nimbus 7 Limb Infrared Monitor of the Stratosphere, *J. Geophys. Res.*, *90*, 10,681–10,692, 1985.

Fomichev, V. I., and J. P. Blanchet, Development of the New CCC/GCM longwave radiation model for extension into the middle atmosphere, *Atmos. Ocean*, *33*, 513–531, 1995.

Fomichev, V. I., J. P. Blanchet, and D. S. Turner, Matrix parameterization of the 15μm CO_2 band cooling in the middle and upper atmosphere for variable CO_2 concentration, *J. Geophys. Res.*, *103*, 11,505–11,528, 1998.

Garcia, R. R., Parameterization of planetary wave breaking in the middle atmosphere, *J. Atmos. Sci.*, *48*, 1405–1419, 1991.

Garcia, R. R., and S. Solomon, The effects of breaking waves on the dynamics and chemical composition of the mesosphere and lower thermosphere, *J. Geophys. Res.*, *90*, 3850–3868, 1985.

Garcia, R. R., F. Stordal, S. Solomon, and J. T. Kiehl, A new numerical model of the middle atmosphere, 1, Dynamics and transport of tropospheric source gases, *J. Geophys. Res.*, *97*, 12,967–12,991, 1992.

Garcia, R. R., T. J. Dunkerton, R. S. Lieberman, and R. A. Vincent, Climatology of the tropical middle atmosphere, *J. Atmos. Sci.*, *102*, 26,019–26,032, 1997.

Gille, J. C., and L. V. Lyjack, An overview of wave-mean flow interactions during the winter of 1978–1979 derived from LIMS observations, in *Dynamics of the Middle Atmosphere*, edited by J. R. Holton and T. Matsuno, 543 pp., D. Reidel, Norwell, Mass., 1984.

Hack, J. J., J. T. Kiehl, and J. W. Hurrell, The hydrological and thermodynamic characteristics of the NCAR CCM3, *J. Clim.*, *11*, 1179–1206, 1998.

Hauchecorne, A., and A. Maillard, A 2-D dynamical model of mesospheric temperature inversions in winter, *Geophys. Res. Lett.*, *17*, 2197–2200, 1990.

Hauchecorne, A., M. L. Chanin, and R. Wilson, Mesospheric temperature inversions and gravity wave breaking, *Geophys. Res. Lett.*, *14*, 933–936, 1987.

Holton, J. R., The influence of graviy wave breaking on the general circulation of the middle atmosphere, *J. Atmos. Sci.*, *40*, 2497–2507, 1983.

Hurrell, J. W., J. J. Hack, B. A. Boville, D. L. Williamson, and J. T. Kiehl, The dynamical simulation of the NCAR Community Climate Model Version 3 (CCM3), *J. Clim.*, *11*, 1207–1236, 1998.

Kiehl, J. T., J. J. Hack, G. B. Bonan, B. A. Boville, D. L. Williamson, and P. J. Rasch, The National Center for Atmospheric Research Community Climate Model, CCM3, *J. Clim.*, *11*, 1131–1149, 1998a.

Kiehl, J. T., J. J. Hack, and J. W. Hurrell, The energy budget of the NCAR Community Climate Model: CCM3, *J. Clim.*, *11*, 1151–1178, 1998b.

Leblanc, T., and A. Hauchecorne, Recent observations of mesospheric temperature inversions, *J. Geophys. Res.*, *102*, 19,471–19,482, 1997.

Leblanc, T., A. Hauchecorne, M. L. Chanin, C. Rodgers, F. Taylor, and N. Livesey, Mesospheric temperature inversions as seen by ISAMS in December 1991, *Geophys. Res. Lett.*, *22*, 1485–1488, 1995.

Lindzen, R. S., Turbulence and stress due to gravity wave and tidal breakdown, *J. Geophys. Res.*, *86*, 9701–9714, 1981.

Liu, H.-L., and M. E. Hagan, Local heating/cooling of the mesosphere due to gravity wave and tidal coupling, *Geophys. Res. Lett.*, *25*, 2941–2944, 1998.

Matsuno, T., A quasi one-dimensional model of the middle atmosphere circulation interacting with internal gravity waves, *J. Meteorol. Soc. Jpn.*, *60*, 215–226, 1982.

McIntyre, M. E., and T. N. Palmer, The "surf zone" in the stratosphere, *J. Atmos. Terr. Phys.*, *46*, 825–849, 1984.

McLandress, C., G. G. Shepherd, B. Solheim, M. D. Burrage, P. B. Hays, and W. R. Skinner, Combined mesosphere/thermosphere winds using WINDII and HRDI data from the Upper Atmosphere Research Satellite, *J. Geophys. Res.*, *101*, 10,441–10,453, 1996.

Meriwether, J. W., P. D. Dao, R. T. McNutt, W. Klemetti, W. Moskowitz, and G. Davidson, Rayleigh lidar observations of mesospheric temperature structure, *J. Geophys. Res.*, *99*, 16,973–16,987, 1994.

Meriwether, J. W., X. Gao, V. B. Wickwar, T. Wilkerson, K. Beissner, S. Collins, and M. E. Hagan, Observed coupling of the mesosphere inversion layer to the thermal tidal structure, *Geophys. Res. Lett.*, *25*, 1479–1482, 1998.

Plumb, R. A., and J. D. Mahlman, The zonally averaged transport characteristics of the GFDL General Circulation/Transport Model, *J. Atmos. Sci.*, *44*, 298–327, 1987.

Roble, R. G., and E. C. Ridley, A Thermosphere-Ionosphere-Mesosphere-Electrodynamics General Circulation Model (TIME-GCM): Equinox solar cycle minimum simulations (30–500km), *Geophys. Res. Lett.*, *21*, 417–420, 1994.

Salby, M., F. Sassi, P. Callaghan, D. Wu, P. Keckhut, and A. Hauchecorne, Mesospheric inversions and their relationship to planetary wave structure, *J. Geophys.*, *107*, doi:2001JD000756, 2001.

Sassi, F., and M. Salby, Diurnal variations in the middle atmosphere observed by UARS, *J. Geophys. Res.*, *104*, 3729–3739, 1999.

Schmidlin, F. J., Temperature inversions near 75 km, *Geophys. Res. Lett.*, *3*, 173–176, 1976.

Williamson, D. L., Climate simulations with a spectral, semi-Lagrangian model with linear grids, in *Numerical Methods in Atmospheric and Ocean Modelling: The André J. Robert Memorial Volume*, edited by C. Lin, R. Laprise, and H. Ritchie, pp. 279–292, Can. Meteorol. and Oceanogr. Soc., Ottawa, Ont., Canada, 1997.

Williamson, D. L., and J. G. Olson, Climate simulations with a semi-Lagrangian version of the NCAR Community Climate Model, *Mon. Weather Rev.*, *122*, 1594–1610, 1994.

Wu, D. L., Mesospheric temperature inversion layers: Recent observations from UARS ISAMS and MLS, *Recent Res. Dev. Geophys.*, *3*, 37–44, 2000.

B. A. Boville, R. R. Garcia, H. Liu, and F. Sassi, National Center for Atmospheric Research, P.O. Box 3000, Boulder, CO 80307, USA. (boville@ucar.edu; rgarcia@ucar.edu; liuh@ucar.edu; sassi@ncar.ucar.edu)